Supporting Information

Adamson and Lim 10.1073/pnas.1308476110

SI Text

1. SI Model Description

1.1. Introduction and Overview. We constructed a model with ordinary differential equations for each of the following species: GlgC-GFP protein ("GFP"), *glgC-gfp* mRNA ("m"), CsrA dimer ("A"), CsrB noncoding RNA ("B"), CsrD ("D"), CsrA–target mRNA complex ("Am"), and the CsrA–CsrB complex ("AB"). The CsrB–CsrD complex ("BD") is also included in later versions of the model. It should be noted that in our model, "B" represents a pair of CsrA binding sites within the CsrB molecule that can be bound by a single CsrA dimer, and thus the CsrA–CsrB complex "AB" represents a CsrA dimer occupying one pair of CsrA binding sites (*SI Text*, section 1.3).

Our model quantitatively and specifically describes the CsrA regulatory cascade. A previously reported model described the general features of repression of target mRNA translation by a protein and CsrA was cited as example (1); however, the reported model did not incorporate any upstream regulators of CsrA (i.e., CsrB or CsrD) (Figs. 3–6) or negative feedback resulting from the repression of CsrD production by CsrA (Fig. 6). The basic assumptions of our model are described in the main text and below.

Initially, we modeled the synthetic CsrA system in which each gene is under the control of a synthetic promoter without any flanking native regulatory sequences (and therefore without negative feedback). This model was constructed in three sequential steps. In the first step, we modeled only the action of CsrA on the target protein concentration ("one-step cascade"). In the second step, we added CsrB to the one-step cascade model, thereby creating a "two-step cascade" model. In the third step, we added CsrD to the two-step cascade model to create a "three-step cascade" model. Parameter values were obtained from the literature, reasonable a priori estimates, and by fitting the simulated dynamics to the experimental data. The latter was used to determine the production rates of CsrA, CsrB, and CsrD in the one-, two-, and three-step cascade models, respectively. The one-, two-, and three-step cascade models were each validated by comparing the transfer functions they predicted to those measured experimentally. Finally, we expanded the three-step cascade to include negative feedback and the saturation of CsrD by CsrB to model the behavior of the native CsrA system.

In each dynamics simulation, we turned on or off the production of one component in the cascade ("modulated component") and measured the effect on the concentrations of all of the other components of the system as a function of time. When we turned on the production of the modulated component (e.g., CsrA), its initial concentration was zero and the initial concentrations of the other species (e.g., *glgC-gfp* mRNA and target protein) were at their steady-state levels in the absence of the modulated component. These steady levels were obtained by simulating the system with the production of the modulated component turned off (e.g., CsrA) and allowing the system to converge to steady state. When we turned off the production of a modulated component (e.g., CsrA), its initial concentration and the initial concentrations of the other species (e.g., *glgC-gfp* mRNA and target protein) were at their steady state with maximal production of the modulated component (i.e., CsrA). These initial steady-state levels (e.g., CsrA, *glgC-gfp* mRNA, and target protein) were obtained by simulating the system with the production of the modulated component turned on (e.g., CsrA) and allowing it to converge to steady state. The simulations were performed by integrating the model's equations using the ode15s solver in MATLAB. All of the initial conditions are provided in Table S1.

The transfer functions were simulated as described above for the dynamics with the production rate of the modulated component (CsrA, CsrB, or CsrD) assigned a range of values between zero (turned off) and its maximum (turned on). For each value of the production rate, we ran the dynamics simulations to convergence to determine the steady-state target protein concentration. We emphasize that the model was constructed from first principles, parameter values obtained from the literature, and production rates obtained from the dynamics experiments. No information from our steady-state experiments was incorporated into the models used to predict the transfer functions. Furthermore, predicting the transfer functions is nontrivial because they convolve multiple nonlinear functions. For example, predicting the effect of varying the steady-state CsrD concentration on the steady-state target protein concentration requires the model to accurately predict how the CsrD concentration alters the CsrB concentration, how the CsrB concentration alters the free CsrA concentration, and how the free CsrA concentration alters the target mRNA's concentration and translation. We performed in vivo experiments to determine the transfer functions and found them to be in good agreement with the predictions. That is, the steady-state experiments confirmed the predictive capacity of our model and thus the appropriateness of its assumptions and parameters.

1.2. One-Step Cascade (CsrA and Target). The simplest model is the "one-step" cascade that contains only target proteins, target mRNAs, CsrA dimers, and CsrA–target mRNA complexes ("CsrA–*glgC* mRNA") (Fig. 2). Our model describes the production and removal (by dilution, active degradation, and/or sequestration) of each component.

The GlgC-GFP concentration ([GFP]) is determined by (*i*) its production rate, which is proportional to the free *glgC-gfp* mRNA concentration ([m]) and the rate constant for translation α_G; and (*ii*) its degradation rate, which is proportional to [GFP] and the sum of the rate constants for passive dilution (β_{dil}) and active degradation of the protein (β_G):

$$\frac{d[\mathrm{GFP}]}{dt} = \alpha_G[\mathrm{m}] - (\beta_G + \beta_{dil})[\mathrm{GFP}]. \qquad \textbf{[S1]}$$

The concentration of free *glgC-gfp* mRNA ([m]) is determined by (*i*) its production rate α_m, which depends on promoter activity; and (*ii*) its removal rate, which depends on passive dilution, active degradation, and sequestration by CsrA. The rates of active degradation and passive dilution for the mRNA are proportional to [m] and the rate constants β_m and β_{dil}, respectively. The rate of removal of free *glgC-gfp* mRNA via sequestration into the CsrA–*glgC* mRNA complex (Am) is proportional to the *glgC-gfp* mRNA and CsrA concentrations and the rate constant for association (k_1). Release of free *glgC-gfp* mRNA from the CsrA–*glgC* mRNA complex is proportional to the concentration of the complex ([Am]) and the dissociation rate constant k_{-1}. For simplicity, we assume the *glgC* leader sequence in the *glgC-gfp* mRNA is capable of binding to one CsrA dimer and that the bound CsrA completely inhibits translation. Because the predictions of our model are in good agreement with our in vivo dynamics data (see main text), this simplifying assumption indicates that more complex modes of interaction between CsrA and RNA molecules

(e.g., cooperativity) are not required to explain the observed dynamics (note: this is modeled and discussed in detail in *SI Text*, section 1.6). In addition, the details of the reaction steps involved in CsrA binding to its RNA partners have not been fully elucidated and are still being investigated (2). Theoretically, free *glgC-gfp* mRNA could also be generated by active degradation of CsrA in the CsrA–*glgC* mRNA complex; although we include this possibility to be systematic, active degradation of CsrA is negligible, and therefore we set the rate constant for this reaction (β_{AAm}) to zero:

$$\frac{d[\mathrm{m}]}{dt} = \alpha_m - (\beta_m + \beta_{dil})[\mathrm{m}] - k_1[\mathrm{A}][\mathrm{m}] + (k_{-1} + \beta_{AAm})[\mathrm{Am}]. \quad \textbf{[S2]}$$

The concentration of CsrA–*glgC* mRNA complex ([Am]) is determined by it creation rate (which depends on the association rate constant and the concentrations of *glgC-gfp* mRNA and CsrA) and the clearance rate [which is proportional to the concentration of CsrA–*glgC* mRNA complex and the rate constants for dissociation (k_{-1}), active degradation of the *glgC-gfp* mRNA within the complex (β_{mAm}), active degradation of CsrA within the complex (β_{AAm}), and passive dilution (β_{dil})]:

$$\frac{d[\mathrm{Am}]}{dt} = k_1[\mathrm{A}][\mathrm{m}] - (k_{-1} + \beta_{mAm} + \beta_{AAm} + \beta_{dil})[\mathrm{Am}]. \quad \textbf{[S3]}$$

The concentration of free CsrA dimer ([A]) is determined by (*i*) its production rate α_A and (*ii*) its removal rate, which depends on passive dilution, active degradation, and sequestration into the CsrA–*glgC* complex. The production of CsrA dimers was treated as a single step to maintain the simplicity of the model. It was unnecessary to explicitly model the production and degradation of *csrA* mRNA because its half-life is short compared with the CsrA protein's half-life (therefore, the dynamics of the *csrA* mRNA has negligible effect on the CsrA protein dynamics). Similarly, we do not separately model the monomeric and dimeric forms of CsrA because the vast majority of intracellular CsrA exists as a dimer (3). Furthermore, because very little CsrA is found in the monomeric form, this implies that it associates rapidly compared with the turnover rate of CsrA. In the unlikely event that CsrA dimerization is slow, its contribution to the dynamics would be accounted for because it would be incorporated into the CsrA production rate α_A, which is obtained from a fit to the experimental data (see below). The rate of removal of free CsrA dimers via active degradation and passive dilution is proportional to [A] and the rate constants β_A and β_{dil}, respectively. We included the possibility of active degradation of CsrA in the model for completeness; however, because CsrA is a stable protein, we assumed β_A to be zero. Free CsrA dimers are removed by sequestration into the CsrA–*glgC* mRNA complex as described above. Free CsrA dimers are generated both by degradation of the *glgC-gfp* mRNA within the CsrA–*glgC* mRNA complex (rate constant β_{mAm}) and by dissociation of the CsrA–*glgC* mRNA complex (rate constant k_{-1}):

$$\frac{d[\mathrm{A}]}{dt} = \alpha_A - (\beta_A + \beta_{dil})[\mathrm{A}] - k_1[\mathrm{A}][\mathrm{m}] + (k_{-1} + \beta_{mAm})[\mathrm{Am}]. \quad \textbf{[S4a]}$$

We now establish numerical values for the above kinetic parameters. The rate constant for passive dilution (β_{dil}) was determined to be 4×10^{-4} s^{-1} by dividing ln(2) by the average doubling time of four strains (HL4495, HL4574, HL4845, and HL4860) grown in LB in the absence of inducer molecules. We used stable GFP in our simulated experiments (i.e., GFP is not actively degraded); therefore, $\beta_G = 0$. We estimated that the steady-state target protein concentration was likely to be on the high end of the physiological range (2×10^2 nM) (4) because the *glgC-gfp* mRNA is transcribed from a strong promoter, the *glgC-gfp* gene is located on a medium copy plasmid, and the *glgC-gfp* mRNA has an efficient ribosome binding sequence (RBS). Multiplying this steady-state concentration of target protein by β_{dil} yields the GFP production rate (8×10^{-2} nM·s^{-1}), which is the product of the rate constant for GFP production (α_G) and the steady-state *glgC-gfp* mRNA concentration. The steady-state *glgC-gfp* mRNA concentration was also estimated to be on the high side of the physiological range (1×10^1 nM) due to its strong promoter and because the gene is on a medium copy plasmid (4). Dividing the total GFP production rate by the steady-state mRNA concentration provides $\alpha_G = 8 \times 10^{-3}$ s^{-1}.

We next specify the rate constants related to the *glgC-gfp* mRNA. We multiplied the steady-state concentration of target mRNA (1×10^1 nM) by the sum of the rate constants for passive dilution (β_{dil}) and active degradation (β_m) to calculate the production rate for the *glgC-gfp* mRNA (α_m). β_m was estimated to be 6×10^{-3} s^{-1} by dividing ln(2) by the half-life (~120 s) determined from reported plots of native *glgC* mRNA degradation (5). Therefore, $\beta_m + \beta_{dil} = 6.0 \times 10^{-3}$ s^{-1} + 0.4×10^{-3} s^{-1} = 6.4×10^{-3} s^{-1} and $\alpha_m = 6.4 \times 10^{-2}$ nM·s^{-1}. We assumed that the active degradation of CsrA, bound or unbound, is negligible; this is supported both by our experiments (Figs. 2*B* and 5) and studies that have shown that the vast majority of intracellular proteins in *Escherichia coli* are stable (6). We therefore assume that the rate constant for active degradation of CsrA from within the CsrA–*glgC* mRNA complex (β_{AAm}) is zero. The rate constants k_1 and k_{-1} are unknown but their ratio ($K_{d,Am} = k_{-1}/k_1$) has been determined for native *glgC* mRNA (~40 nM) (7). We used the association rate constant for another RNA–protein complex (a 16-nt RNA substrate binding to Hfq) (8), which has been determined (~10^{-1} nM^{-1}·s^{-1}), as a starting point for estimating k_1. Thinking ahead, the association rate constant of the CsrA–CsrB complex is likely to be larger than that of the CsrA–*glgC* mRNA complex due to the difference in their reported K_d values (see below). We therefore selected a conservative value for the association rate constant of the CsrA–*glgC* mRNA complex (k_1 = 10^{-2} nM^{-1}·s^{-1}), leaving the higher value for the association rate constant of the CsrA–CsrB complex (10^{-1} nM^{-1}·s^{-1}). Having estimated k_1, we calculated $k_{-1} = 4 \times 10^{-1}$ s^{-1} from the above ratio (k_{-1}/k_1 ~40 nM). The rate constant for the active degradation of *glgC-gfp* mRNA from within the CsrA–*glgC* mRNA complex ($\beta_{mAm} = 2 \times 10^{-2}$ s^{-1}) was calculated by dividing ln(2) by the half-life (~35 s) estimated from plots of the degradation of native *glgC* mRNA bound to CsrA (5).

We now establish the remaining rate constants for CsrA that have not been described above. As we discussed, CsrA is not believed to be actively degraded; therefore, $\beta_A = 0$ s^{-1}, and therefore, CsrA is cleared at a rate determined by β_{dil}. The value for the production rate of CsrA dimer, α_A (2×10^{-2} nM·s^{-1}), was determined by fitting the model to our dynamics data. Specifically, α_A was selected so that the simulated delay in turning on target expression caused by turning off *csrA* transcription (which depends on the CsrA concentration) was comparable in magnitude to that measured experimentally (Fig. 2*B*).

Simulation of the one-step cascade with the above parameters and only a single fit parameter (α_A) was able to describe the dynamics behavior of the system with CsrA production turned off ($\alpha_A = 0$; Fig. 2*B*) or on ($\alpha_A = 2 \times 10^{-2}$ nM·s^{-1}; Fig. 2*C*). Furthermore, simulation of the system with a range of different CsrA production rates ($0 \le \alpha_A \le 2 \times 10^{-2}$ nM·s^{-1}) qualitatively predicted the steady-state CsrA transfer function (Fig. 2*D*).

1.3. Two-Step Cascade (CsrB, CsrA, and Target). The two-step cascade model extends the one-step cascade to include CsrB and the CsrA–CsrB complex (Fig. 3). This model is described by Eqs. **S1–S3**, **S4b**, **S5a**, and **S6**. The concentration of free CsrB ([B]) is determined by its (*i*) production rate α_B and (*ii*) removal rate

due to passive dilution, active degradation (via non-CsrD pathways), and sequestration into the CsrA–CsrB complex. For simplicity, [B] represents the concentration of CsrB binding sites rather than the concentration of full-length CsrB RNA molecules. In other words, we measure the CsrB concentration in terms of CsrA dimer equivalents where one unit of CsrB can bind one CsrA dimer. This assumes that the binding of each CsrA dimer to CsrB is independent, which is the simplest model. More complex binding interactions between CsrA and CsrB are unnecessary for qualitative agreement between our model and experimental measurements (*SI Text*, section 1.6 and Figs. 2–4). To be clear, we refer to the independent binding of CsrA dimers to CsrB not to the binding of the individual CsrA molecules within a dimer to CsrB. In the latter case, the binding of a CsrA molecule within a dimer to CsrB is known to increase the probability that the other CsrA molecule will also bind to CsrB (2); this behavior is included in our model with the assumption that CsrA dimers occupy two binding sites within CsrB (i.e., CsrB has 18 sites for CsrA, but only 9 sites for CsrA dimers).

As with all other species in our model, the rate of passive dilution of CsrB is proportional to its concentration and the rate constant β_{dil}. The rate of active degradation of CsrB via non–CsrD-mediated pathways is proportional to [B] and the rate constant β_B. The rate of sequestration of CsrB is proportional to [B], [A], and the association rate constant for the CsrA–CsrB complex (k_2). CsrB can be released from the CsrA–CsrB complex by active degradation of CsrA or by dissociation; the rates of these reactions are proportional to the concentration of the complex ([AB]) and the constants β_{AAB} or k_{-2}, respectively. Active degradation of CsrB in the CsrA–CsrB complex may also generate free CsrA at a rate that is proportional to the concentration of the complex ([AB]) and the rate constant β_{BAB}.

A model of CsrB molecules with nine sites for CsrA dimers versus a model of single binding sites for CsrA dimer will produce equivalent results in a deterministic model. However, the latter is much simpler because there is no need to model all of the different types of CsrA–CsrB complexes. The reason the two types of models are equivalent is that differences in the production rate are taken into account when we fit this parameter. Furthermore, the degradation rate constants for CsrB molecules and individual CsrA dimer binding sites, which depend on their lifetimes, are the same under conditions where CsrB clearance is not saturated. That is, under nonsaturating conditions, the time taken to cleave an individual molecule is independent of the number of other molecules present. Under these circumstances, the rate of clearance of single CsrA dimer sites will be nine times greater than for CsrB whole molecules but the rate constant and overall flux of dimer sites is identical. Under conditions when CsrD is saturated with CsrB, we fit our model to the experimental data, and therefore, the parameter values obtained account for differences in the clearance of CsrB molecules and single binding sites for CsrA dimer.

The equations for the two-step cascade include the above process as well as those described in the one-step cascade; that is, Eqs. **S1–S3** from the one-step cascade and a modified equation for the free CsrA concentration (Eq. **S4b**) that includes the association, dissociation, and active degradation of the CsrA–CsrB complex:

$$\frac{d[A]}{dt} = \alpha_A - (\beta_A + \beta_{dil})[A] - k_1[A][m] + (k_{-1} + \beta_{mAm})[Am] - k_2[A][B] + (k_{-2} + \beta_{BAB})[AB]. \quad \textbf{[S4b]}$$

In addition, the model for the two step cascade has equations for free CsrB and the CsrA–CsrB complex:

$$\frac{d[B]}{dt} = \alpha_B - (\beta_B + \beta_{dil})[B] - k_2[A][B] + (k_{-2} + \beta_{AAB})[AB]; \quad \textbf{[S5a]}$$

$$\frac{d[AB]}{dt} = k_2[A][B] - (k_{-2} + \beta_{BAB} + \beta_{AAB} + \beta_{dil})[AB]. \quad \textbf{[S6]}$$

The values of the additional parameters were obtained as follows. CsrB stability is not believed to be affected by binding to CsrA (9) (unlike target mRNAs that bind to CsrA), and therefore, the active degradation rates for bound and unbound CsrB are the same ($\beta_{BAB} \equiv \beta_B$). The rate constant for the active degradation of CsrB in the absence of CsrD ($\beta_B \leq 4 \times 10^{-4}$ s^{-1}) was determined by dividing ln(2) by the reported half-life of CsrB (≥30 min) in a *csrD* deletion strain (10). It is unclear how much the half-life was influenced by cell growth; therefore, the above value should be considered as an upper bound. In other words, active degradation contributes the same or less than passive dilution to the clearance of CsrB. We include the active degradation of CsrA from the CsrA–CsrB complex (β_{AAB}) for completeness. However, because CsrA is stable, $\beta_{AAB} = 0$. The association rate constant for CsrA dimer binding to CsrB (k_2) was estimated to be similar in magnitude to RNA binding to Hfq (see above; $k_2 = 10^{-1}$ nM^{-1}·s^{-1}). We calculated the dissociation rate constant for the CsrA–CsrB complex ($k_{-2} = 10^{-1}$ s^{-1}) from the above value for k_2 and the reported equilibrium dissociation constant for this complex ($K_{d,AB} = k_{-2}/k_2 \sim 1$ nM) as measured by gel mobility shift assays (11). The production rate of pairs of CsrB binding sites ($\alpha_B = 4$ nM·s^{-1}) was determined by fitting the model to our dynamics data so the simulated signaling delay was comparable in magnitude to that measured experimentally (Fig. 3*C*). This production rate corresponds to a steady-state concentration of CsrB binding sites [B] of 5×10^3 nM. Because each CsrB molecule has approximately nine binding sites for CsrA dimers (assuming both faces of the CsrA dimer bind simultaneously) (12), the concentration of CsrB molecules will be approximately ninefold lower than [B] (and therefore the production rate for CsrB molecules would also be ninefold lower).

Simulation of the two-step cascade with the above parameters and only a single fit parameter (α_B) was able to describe the dynamics behavior of the system with CsrB production turned on ($\alpha_B = 4$ nM·s^{-1}; Fig. 3*B*) or off ($\alpha_B = 0$; Fig. 3*C*). Furthermore, simulation of the system with a range of different CsrB production rates ($0 \leq \alpha_B \leq 4$ nM·s^{-1}) qualitatively predicted the steady-state CsrB transfer function (Fig. 3*D*).

1.4. Three-Step Cascade (CsrD, CsrB, CsrA, and Target). The three-step cascade model extends the two-step cascade to include CsrD (Fig. 4). This model is described by Eqs. **S1–S3**, **S4b**, **S5b**, **S6**, and **S7a**. The concentration of CsrD ([D]) depends on (*i*) its production rate (α_D) and (*ii*) its removal rate by passive dilution and active degradation. The production of CsrD is modeled as a single reaction step as with CsrA dimers. The clearance of CsrD by passive dilution and active degradation is proportional to [D] and the rate constants β_D and β_{dil}, respectively:

$$\frac{d[D]}{dt} = \alpha_D - (\beta_D + \beta_{dil})[D]. \quad \textbf{[S7a]}$$

CsrD is known to bind to and facilitate the degradation of free CsrB by RNase E (10). The kinetics of this process has not been completely characterized, and therefore we begin by modeling the action of CsrD as a simple first-order process. Active degradation of free CsrB by CsrD is therefore proportional to [B], [D], and a single kinetic parameter that defines the catalytic efficiency of CsrD-mediated degradation (ω). Incorporating active degradation of CsrB by the CsrD-mediated pathway into the model converts Eq. **S5a** into Eq. **S5b**:

$$\frac{d[B]}{dt} = \alpha_B - (\omega[D] + \beta_B + \beta_{dil})[B] - k_2[A][B] + (k_{-2} + \beta_{AAB})[AB]. \quad \textbf{[S5b]}$$

This equation assumes the free CsrB concentration is not greatly in excess of the CsrD concentration, which our experiments show is appropriate for dynamics experiments using the synthetic CsrA cascade (Fig. 4). However, at the lower concentrations of CsrD that can occur with native *csrD* (Fig. 6 *B*, *C*, *E*, and *G*) or at very low induction levels of synthetic *csrD* (Fig. 6*F*), CsrD can become saturated by high levels of free CsrB. Under these conditions in which CsrD becomes saturated, it is important to consider the CsrB–CsrD complex (see next section). As stated above, the three-step cascade model combines all of the equations for the two-step cascade except Eq. **S5a** (i.e., Eqs. **S1**, **S2**, **S3**, **S4b**, and **S6**) plus Eqs. **S5b** and **S7a**.

The additional parameter values for Eqs. **S5b** and **S7a** were determined as follows. It is believed that CsrD is primarily cleared by dilution for the same reasons as CsrA; therefore, the rate constant for active degradation of CsrD is assumed to be near zero ($\beta_D = 0$). Because CsrD partners with RNase E to degrade CsrB, we selected a catalytic efficiency value ($\omega = 8 \times 10^{-3}$ nM^{-1}·s^{-1}) within the range of reported catalytic efficiencies for RNase E (13, 14). The production rate for CsrD ($\alpha_D = 8 \times 10^{-2}$ nM·s^{-1}) was determined by fitting the model to our dynamics data so that the simulated signaling delay was comparable in magnitude to that measured experimentally (Fig. 4*B*). It should be noted that all other parameter values (including α_A and α_B) were held fixed during this fit process. We found the production rate for CsrD is less than that for CsrA, which is consistent with *csrD* having a weaker ribosomal binding sequence (st3 instead of the stronger st7 ribosomal binding sequence of synthetic *csrA*) (15).

Simulation of the three-step cascade with the above parameters and only a single fit parameter (α_D) was able to describe the dynamic behavior of the system with CsrD production turned off ($\alpha_D = 0$; Fig. 4*B*) or on ($\alpha_D = 8 \times 10^{-2}$ nM·s^{-1}; Fig. 4*C*). Furthermore, simulation of the system with a range of different CsrD production rates ($0 \le \alpha_D \le 8 \times 10^{-2}$ nM·s^{-1}) qualitatively predicted the CsrD transfer function at steady state (Fig. 4*D*).

1.5. Three-Step Cascade with Feedback. To interpret and explain our experimental observations for the CsrA cascade with native *csrD*, we incorporated into our model the repression of CsrD production by CsrA (Fig. 6). This repression is necessary for negative-feedback regulation. Because native *csrD* is not as highly expressed as synthetic *csrD*, CsrD may become saturated by CsrB; therefore, we needed to explicitly include CsrB–CsrD complexes (BD) in the model to account for this possibility. The model verified that negative feedback was necessary for the "enhanced signaling" observed in Fig. 6*E*. In addition, the model demonstrated that saturation of CsrD activity by CsrB is required for the delay observed in Fig. 6*F*. The delay does not occur if CsrD is absent (Fig. 6*F*) or with low constant expression of CsrD without saturation (Fig. S4*F*).

The repression of CsrD expression by CsrA was incorporated into the model by having the production rate of CsrD from native *csrD* depend on the CsrA concentration according to a simple Hill-type function. The Hill-type function (16) is $k_f/(k_f + [A])$, where the constant k_f determines the CsrA concentration [A] at which CsrD production is one-half of its maximum value. Use of the Hill-type function requires fewer parameters and assumptions than additional equations that explicitly consider the *csrD* mRNA and its association, dissociation, degradation, and translation in the CsrA–*csrD* mRNA complex (note: to our knowledge, this complex has not been identified in vivo).

The association of CsrB and CsrD results in the CsrB–CsrD complex, and this reaction occurs at a rate proportional to [B], [D], and the rate constant k_{ES}. The CsrB–CsrD complex dissociates to free CsrB and CsrD at a rate that depends on its concentration and the rate constant k_{-ES}. Clearance of the CsrB–CsrD complex can occur by dilution, active degradation of CsrB in the complex by RNase E (which releases free CsrD), and active degradation of CsrD in the complex (which releases free CsrB); the rate constants for these respective processes are β_{dil}, k_P, and β_D.

Our model of the three-step cascade with feedback regulation extends the previous model to include (*i*) the regulation of CsrD production by CsrA and (*ii*) the addition of an equation for the CsrB–CsrD complex. The final set of equations for the three-step model with feedback is therefore the following:

$$\frac{d[GFP]}{dt} = \alpha_G[m] - (\beta_G + \beta_{dil})[GFP], \quad \textbf{[S1]}$$

$$\frac{d[m]}{dt} = \alpha_m - (\beta_m + \beta_{dil})[m] - k_1[A][m] + (k_{-1} + \beta_{AAm})[Am], \quad \textbf{[S2]}$$

$$\frac{d[Am]}{dt} = k_1[A][m] - (k_{-1} + \beta_{mAm} + \beta_{AAm} + \beta_{dil})[Am], \quad \textbf{[S3]}$$

$$\frac{d[A]}{dt} = \alpha_A - (\beta_A + \beta_{dil})[A] - k_1[A][m] + (k_{-1} + \beta_{mAm})[Am] - k_2[A][B] + (k_{-2} + \beta_{BAB})[AB], \quad \textbf{[S4b]}$$

$$\frac{d[B]}{dt} = \alpha_B - (\beta_B + \beta_{dil})[B] - k_2[A][B] + (k_{-2} + \beta_{AAB})[AB] - k_{ES}[B][D] + (k_{-ES} + \beta_D)[BD], \quad \textbf{[S5c]}$$

$$\frac{d[AB]}{dt} = k_2[A][B] - (k_{-2} + \beta_{BAB} + \beta_{AAB} + \beta_{dil})[AB], \quad \textbf{[S6]}$$

$$\frac{d[D]}{dt} = \alpha_D\left(\frac{k_f}{k_f + [A]}\right) - (\beta_D + \beta_{dil})[D] - k_{ES}[B][D] + (k_{-ES} + k_P)[BD], \text{ and} \quad \textbf{[S7b]}$$

$$\frac{d[BD]}{dt} = k_{ES}[B][D] - (\beta_D + k_{-ES} + k_P + \beta_{dil})[BD]. \quad \textbf{[S8]}$$

The parameter values used to simulate the dynamics of the three-step cascade with feedback were identical to those used in the three-step cascade without feedback unless otherwise stated. The additional parameters values that were not in the original three-step cascade without feedback model (i.e., k_f, k_{ES}, k_{-ES}, and k_P) were determined as follows. We estimated k_{ES} (the association rate constant for the binding of CsrB to CsrD) to be the same as the association rate constant between CsrB and CsrA ($k_{ES} = k_2 = 10^{-1}$ nM^{-1}·s^{-1}). k_P, k_{-ES}, k_f, and α_D were obtained by simultaneously fitting the model to the dynamic behavior of the experimental results in Fig. 6 *B*–*G*. Identical values for k_P and k_{-ES} were used for all simulations in Fig. 6. The value for the rate constant for the conversion of CsrB–CsrD complex into free CsrD and degraded CsrB ($k_P = 8 \times 10^{-2}$ s^{-1}) falls within the experimentally measured range reported for RNase E [3×10^{-2} s^{-1} (13) to 1.4 s^{-1} (14)]. Our value for the rate constant for CsrB dissociation from CsrD (k_{-ES}) was 2×10^{-2} s^{-1}, which is comparable to reported RNA–protein dissociation rate constants (17-19).

k_f pertains only to the simulations demonstrating the effects of feedback (dark and light blue lines in Fig. 6*E* and gold line in Fig. 6*G*); its value (k_f = 30 nM) was identical in all three simulations and was comparable to the levels of free CsrA observed in the model. We estimate that the level of CsrA produced by the native *csrA* gene to be approximately 1/10th the concentration that we expressed in our synthetic system (Fig. 2*D*). Therefore, $\alpha_D = 8 \times 10^{-2}$ nM·s^{-1} for the native *csrA* gene (0.1× CsrA; Fig. 6*E* and Fig. S1) and $\alpha_D = 8 \times 10^{-1}$ nM·s^{-1} for the synthetic *csrA* gene (1× CsrA; Fig. 6*E* and Fig. S1).

Simulations of the three-step cascade with feedback using the above parameters were able to describe the dynamic behavior of the system. In the models, we turned *csrB* transcription either on (Fig. 6 *B–F*) or off (Fig. 6*G*) under different combinations of conditions. These conditions include two different CsrA concentrations: (*i*) native CsrA levels ($\alpha_A = 8 \times 10^{-2}$ nM·s^{-1}; light blue line in Fig. 6*E* and gold line in Fig. 6*G*) or (*ii*) synthetic CsrA levels ($\alpha_A = 8 \times 10^{-1}$ nM·s^{-1}; dark blue line in Fig. 6*E* and magenta line in Fig. 6*F*, and black line in Fig. 6 *E–G*). We also modeled three possible regulatory patterns for CsrD: (*i*) no expression ($\alpha_D = 0$; black control curve in Fig. 6 *E–G*), (*ii*) low induced expression without feedback ($\alpha_D = 1.16 \times 10^{-2}$ nM·s^{-1}; magenta curve in Fig. 6*F*), and (*iii*) native expression with feedback ($\alpha_D = 1.6 \times 10^{-1}$ nM·s^{-1}; gold line in Fig. 6 *B* and *G*, orange line in Fig. 6*C*, and blue line in Fig. 6*E*). In the case of the low induced expression of CsrD without feedback (Fig. 6*F*), the term $\alpha_D \cdot (k_f/(k_f + [A]))$ in the model was replaced with just α_D. The low expression of CsrD was achieved experimentally (Fig. 6*F*) from PLlacO-1 by adding 20 μM IPTG to the media rather than the 0.5–1 mM IPTG required for full transcription (Fig. S2*Q*). The maximum production rates for *glgC-gfp* mRNA (α_m), GlgC-GFP protein (α_{gfp}), and CsrB (α_B) are the same in Fig. 6 *E–G* as described in prior sections.

1.6. Cooperative CsrA Binding Has Minimal Effect on the Dynamics and Transfer Function. In our model, CsrA binds as a dimer to its target mRNAs and noncoding RNAs. This feature of the model is based on experimental evidence showing that CsrA primarily exists in the cell as a dimer (3). It has also been shown experimentally that an individual CsrA subunit can facilitate the binding of its dimer partner to CsrB (2); this phenomenon is included in our model in that we assume that both CsrA molecules in the dimer bind together to CsrB. One CsrA molecule facilitating the binding of the other CsrA molecule within the same dimer is distinct from cooperative binding between CsrA dimers in which the binding of one CsrA dimer promotes the binding of another CsrA dimer to CsrB or an mRNA. There is one report that may indicate cooperative binding of CsrA dimers to CsrB (11); however, many details remain unclear. The binding of CsrA dimers to the CsrB noncoding RNA is likely to be very different to that of a small molecule binding a protein. When a small molecule binds to a protein (e.g., dioxygen binding to hemoglobin), it can induce a conformational change in the protein that alters small molecule binding at other sites on the protein. For the CsrB noncoding RNA, there is no described mechanism by which the binding of a CsrA dimer at one location on CsrB enhances the binding of other CsrA dimers at other locations on CsrB, although it is of course possible that this does occur.

In this section, we explore how cooperative binding between CsrA and CsrB would affect the transfer function (Fig. S4*G*) and dynamic behavior (Fig. S4*H*) of our system. To evaluate the effects of cooperativity in CsrB binding on the CsrB transfer function, we compared a model in which each site for a CsrA dimer was bound independently (i.e., "noncooperative") to a model in which the binding of each dimer increased the equilibrium association constant for the binding of the next CsrA dimer by twofold (i.e., "cooperative"). In the noncooperative model, there are nine sites for CsrA dimers on each CsrB molecule and the binding of each CsrA dimer to each site on CsrB is independent. In the cooperative model, there are also nine sites for CsrA dimers on each CsrB molecule; however, in this case, the binding of the first CsrA dimer increases the association rate constant of the second CsrA dimer by twofold, which increases the association rate constant of the third CsrA dimer by a further twofold, and so on until the ninth and last CsrA dimer has an association rate constant that is 2^8-fold greater than that of the first CsrA dimer. In the noncooperative and cooperative models, we varied the total CsrB concentration and measured the amount of free target mRNA in the presence of fixed total CsrA (Fig. S4*G*). Cooperativity is often considered from the perspective of its effect on the steepness of an input–output relationship. In this case, we will quantify the effect of cooperative binding on the change in the free target mRNA concentration (output) as the CsrB concentration (input) increases. We measured the steepness of each function using the "response coefficient" (i.e., the input value that yields 90% of maximum output divided by the input value that yields 10% of maximum output) and then converted these values to an equivalent Hill coefficient as described by Goldbeter and Koshland (20).

We found that the extreme example of cooperative binding described above only increased the Hill coefficient for the CsrB transfer function from 3.7 (for noncooperative binding) to 4.5 (cooperative binding) (Fig. S4*G*). By comparison, a twofold increase in the total CsrA concentration in the system with noncooperative binding increased the Hill coefficient from 3.7 to 5.0. Cooperativity has such a comparatively small effect on the transfer function because the stoichiometric point (where the number of CsrA dimers equals the number of available sites for those dimers on CsrB) creates a sharp transition even in the absence of cooperativity. That is, when the concentration of CsrB sites [B] is less than the CsrA dimer concentration [A], there is substantial silencing of the target mRNA; however, when the concentration of CsrB sites [B] is greater than the CsrA dimer concentration [A], there is minimal silencing of the target mRNA. The sharpness of this transition across the stoichiometric point (from silencing to nonsilencing) depends on the equilibrium dissociation constants for CsrA dimers binding to CsrB sites, and on the absolute concentrations of CsrA dimers and CsrB sites. The transfer function for CsrB is very different from that of a protein acting "catalytically" (e.g., an enzyme or transcription factor) where there is no stoichiometric point and cooperative binding can have a much greater impact on the steepness of the transfer function.

We next compared signaling dynamics using a version of our two-level cascade model that was modified to incorporate cooperative and noncooperative binding as described above. Using this model, we turn on and off *csrB* transcription and monitor target protein levels (Fig. S4*H*) as we did previously (Fig. 3 *B* and *C*). The dynamic behavior of the system with cooperative binding was found to be very similar to the system with noncooperative binding (Fig. S4*H*). Note: cooperative binding implemented by changing dissociation rate constants (rather than association rate constants) produced dynamics traces that are visually indistinguishable from those produced by changing the association rate constants.

In summary, our model demonstrates that the qualitative dynamic behavior of our system can be explained without incorporating cooperative binding. Furthermore, our simulations show that, if the binding of CsrA dimers is cooperative, it is unlikely to have a substantial qualitative effect on the transfer functions or dynamic behavior of the CsrA system.

2. SI Experiments

2.1. Steady-State Measurement of CsrA Repression of CsrD Production by Quantitative RT-PCR. In the main text, we examined feedback by measuring the dynamic response of the CsrA system (Fig. 6) and determined that the only component that had a significant effect

on the dynamics was CsrD. In particular, the data indicated that the inhibition of CsrD expression by CsrA increased the speed of the system's response to changes in CsrB transcription ("enhanced signaling"). Here, we evaluate this feedback regulation of CsrD by CsrA under steady-state conditions.

We measured CsrD mRNA concentrations in parallel for two strains (HL5944 and HL5947) by quantitative RT-PCR. One strain carried a gene that constitutively expressed synthetic *csrA* (HL5947), whereas a second strain contained a control plasmid without *csrA* (HL5944). In the strain expressing CsrA, CsrD mRNA levels were very low [$-9.28 \times 10^{-8} \pm 3.90 \times 10^{-7}$ arbitrary units (a.u.), eight samples, uncertainty is the SEM] and indistinguishable from background (i.e., plus RT measurements were the same as the minus RT control, which contains the harvested RNA but without reverse transcriptase). In contrast, the strain lacking CsrA had significantly elevated CsrD mRNA levels ($1.82 \times 10^{-6} \pm 8.13 \times 10^{-7}$ a.u., eight samples, uncertainty is the SEM). The difference between these two measurements is statistically significant (two-tailed t test: $P = 0.04$, t value = 2.26). We note that the variances of the values for the two strains were not found to be different (Levene's test: $P = 0.26$), so homoscedasticity was assumed for the t test calculation. Our observed decrease in the *csrD* mRNA concentration in the presence of CsrA suggests that CsrD mRNA levels are directly or indirectly repressed by CsrA; this result is consistent with CsrD mRNA measurements from a previous report (21).

In summary, in this study we have demonstrated via two independent types of experiments (dynamics measurements and steady-state RT-PCR) that CsrA represses CsrD production, and these findings are in agreement with prior measurements by others (21).

2.2. Active Versus Passive Clearance of Target Protein Reporters. To determine whether an actively degraded reporter would improve our ability to resolve differences in signaling delays, we repeated some of the dynamics experiments (Figs. 2*C*, 3*C*, and 4*C*) using a destabilized form of GFP as a reporter. These additional experiments with destabilized GFP (Fig. S4 *B*–*E*) were performed identically to those with stable GFP (i.e., Figs. 2*C*, 3*C*, and 4*C*) except the measurements were performed more frequently and for a shorter length of time (protocol in *SI Text*, section 3.2, below). Specifically, we used GlgC-GFP-LVA, which has the LVA degradation tag fused to the C-terminal end of GlgC-GFP (22) (Fig. S4 *B*–*E*). The LVA degradation tag decreased the half-life of the GlgC-GFP target protein by as much as 3.8 ± 0.5-fold relative to the untagged target (Fig. S4 *A* and *B*).

To determine the effect of destabilizing the target protein on our ability to resolve differences between the time delays caused by direct and indirect signaling, we make use of the metric δ:

$$\delta = \tau_{80(\text{indirect})} - \tau_{80(\text{direct})}. \qquad \textbf{[S9]}$$

In Eq. **S9**, $\tau_{80(\text{indirect})}$ is the time delay to reach 80% of the maximum expression with (*i*) CsrA turned off, (*ii*) CsrB turned on, or (*iii*) CsrD turned off, and $\tau_{80(\text{direct})}$ is the time delay to reach 80% of maximum expression after the *glgC-gfp* control is turned off. We found the δ values were similar with stable and destabilized GFP when CsrA is turned off (-1 ± 3 and -2 ± 5 min, respectively), CsrB is turned on (54 ± 3 and 44 ± 7 min, respectively), and CsrD is turned off (3 ± 2 and 7 ± 11 min, respectively) (Table S2 and Fig. S4 *C*–*E*). In short, the addition of a degradation tag to the GFP protein did not improve the measurement of signaling delays.

The dynamics measurements with the LVA-tagged reporter also revealed that its clearance rate is more complicated than that of stable GFP. The clearance of stable GFP by dilution has a clear first-order dependence on reporter concentration (as shown by the linear decrease in fluorescence on the log-linear time course plot in Fig. S4*A*). In contrast, the active clearance of LVA-tagged GFP is slow initially and depends on the starting concentrations of the target protein (Fig. S4*B*). This finding is not unexpected given that active degradation requires specific enzymes and cellular machinery (such as tail-specific proteases) that can become saturated if there are high concentrations of substrate such as GlgC-GFP-LVA. Therefore, the addition of the LVA tag introduces extra complexity into the dynamic behavior of the reporter, and as a consequence the τ values may convolve delays caused by the CsrA cascade with those caused by the target protein degradation machinery. In summary, stable GFP provides a more suitable target protein to isolate the dynamic properties of the CsrA cascade because its clearance is highly predictable and the measured time delays reflect only the delays incurred by the CsrA cascade. In addition, using destabilized GFP to measure time delays was found to increase the uncertainty in our experiments (Table S2).

These experiments demonstrated that LVA-tagged GFP was not the best available choice for measuring dynamics within the CsrA cascade. However, the fact that we have observed similar time delays using experiments with the stable and destabilized GFP demonstrates that the time delays that we have measured in the CsrA system are general and applicable to target proteins that have short lifetimes as well as those that are stable.

3. SI Methods

3.1. Quantitative RT-PCR. Total RNA was extracted from eight exponentially growing cell cultures for each strain (HL5944 and HL5947) using the RNeasy RNA extraction kit (Qiagen). The RNA was treated with DNase I and cDNA was synthesized using the iScript select cDNA synthesis kit and random primers (Bio-Rad). Quantitative RT-PCR was performed to determine the concentration of cDNA using iQ SYBR Green Supermix and the iQ5 Real-Time PCR detection system (Bio-Rad). Samples without reverse transcriptase ("minus RT") were created and measured in parallel to determine the concentration of any contaminating DNA and nonspecific amplification. The reported amount of CsrD mRNA for each sample represents the difference between the amount of cDNA in the RNA sample prepared with reverse transcriptase and the same RNA sample prepared identically except without reverse transcriptase. CsrD mRNA was amplified using the oligonucleotides CsrDinF and CsrDinR (Table S4).

3.2. Dynamics Measurements with Destabilized GFP. Dynamics experiments using destabilized GFP (Fig. S4 *B*–*E*) were performed and measured as described in the main text for stable GFP except that 5–50 μM of overnight culture was inoculated into 10 mL of LB with 100 μg/mL ampicillin and 50 μg/mL kanamycin with IPTG (0.01–1 mM), aTc (1 μM), both or neither. Cells were grown for 3.5 h, centrifuged (16,000 × *g* for 1 min), the supernatant discarded, and the pellets resuspended in 15 mL of fresh media to produce a final $OD_{600} = 0.01$–0.05 and a volume of ∼15 mL. The culture was then grown for 90 min with cells harvested every 10 min. No serial dilution was necessary due to the shortened experimental time frame.

3.3. Strain and Plasmid Construction. The chromosomal genes and operons *csrA*, *csrB*, *csrC*, *csrD*, *glgCAP*, and/or *pgaABCD* were deleted from the chromosome using the λ-red method (23) or removed from their host strain via phage transduction. All deletions were confirmed by PCR. The *csrA* deletion was performed after *glgCAP* was deleted because CsrA is essential for cell survival when *glgCAP* is present (24). CsrA was also deleted only after *pgaABCD* was deleted because in the absence of CsrA, cells with the *pgaABCD* operon overproduced biofilm adhesins (25), which prevented their resuspension and further genetic manipulation.

Plasmid maps are shown in Fig. S5 and oligonucleotide sequences are in Table S4. PconNoHind, PconNoHindM2, and PconNoHindM12 are variants of Pcon/O3 (26) without a HindIII site. The PconNoHindM2 promoter is the same as PconNoHind except for a substitution mutation at the −10 site that modestly increases transcription. The PconNoHindM12 promoter is the same as PconNoHind except for two substitution mutations at the −10 and −35 sites that moderately decrease transcription. The PLlacO-1 and PLtetO-1 promoters and T1 terminators were obtained from the pZ system (27). The st2, st3, and st7 RBS sequences (15) were synthesized. The *gfp* gene and the T1T2 terminator sequence were obtained from pTAK102 (28). The Asp terminator sequence was PCR-amplified from pLex (Invitrogen). The sources and sequences for *tetR* and *lacIq* have been reported (29, 30). *csrA*, *csrB*, *csrC*, and *csrD* genes were PCR amplified from *E. coli* MG1655 chromosomal DNA (Yale *E. coli* Stock Center, CGSC #7740). The *mCherry* gene was amplified from a plasmid provided by R. Tsien (University of California, San Diego, La Jolla, CA) (31).

4. SI Analysis

4.1. Dynamics Measurements with Destabilized GFP. In the dynamics experiments we measure the change in target expression as a function of time after an input (e.g., *csrB* transcription) has been altered at $t = 0$. The change in gene expression reflects the convolved effects of the following: (*i*) the target protein degradation rate, (*ii*) the ratio of the initial and final steady states for the target protein (i.e., dynamic range), and (*iii*) the time required for the CsrA cascade upstream of the target protein to reach equilibrium (30). We eliminate the first factor as a cause for any differences in the dynamics of different CsrA systems by only directly comparing systems that the same target protein. We eliminate the second factor by rescaling the difference between the initial and final steady states so that it is the same for all experiments; specifically, we set the minimum and maximum relative steady-state levels of target expression to 0 and 1, respectively ("zero-to-one rescaling"). By eliminating the first and second factors as possible causes for differences in the time delay for different cascades, we are left with a metric that primarily measures the time required for the CsrA cascade upstream of the target protein to reach equilibrium (Figs. 2–4 and Fig. S2 *A*–*H*).

In all of our dynamics experiments, we had duplicate "physiological" control samples where target protein was constitutively expressed (i.e., GlgC-GFP was on before $t = 0$ and it was maintained in the on state for the duration of the dynamics experiment) (Fig. S2). These control samples are included to demonstrate that conditions are constant (e.g., cell density and inducer activity) throughout the experiment and that there are no changes in nonspecific physiological factors that generally affect gene expression (e.g., ribosome concentration). Moreover, if there is a change in these general factors that affect gene expression, we can correct for them using these control samples, which are measured in parallel.

In purely synthetic systems using stable GFP, the physiological control samples showed only a small amount of "drift" over the course of the dynamics experiments, and therefore there was no need to correct for it (Fig. S2 *A*–*H*). In systems with native genes (Fig. S2 *I*–*P*) or with destabilized GFP (Fig. S4 *C*–*E*), the drift was large compared with the dynamic range (i.e., ratio of maximum to minimum steady-state expression) of the target protein. To correct for this drift, we performed a "point-to-point" normalization (before the zero-to-one rescaling) where the fluorescence value at each time point for each sample was normalized by the fluorescence value in the corresponding physiological control samples at the same time point. This point-to-point normalization was important for HL5860, HL5877, and HL5878 (Fig. S2 *J*, *K*, and *M*) to prevent drift from exaggerating the observed overshoot (Fig. 6 *B*, *C*, and *E*).

4.2. Transfer Function Calibration. We collected our in vivo transfer function data by varying the amount of IPTG and aTc added to the media to induce different levels of expression of CsrA, CsrB, and CsrD from the PLlacO-1 and PLtetO-1 promoters. We then measured the effect of this induction on target protein expression via GFP fluorescence (Figs. 2*D*, 3*D*, and 4*D*). To estimate the relative rate of production of CsrA, CsrB, and CsrD from the PLlacO-1 and PLtetO-1 promoters at each concentration of inducer, we expressed GFP under these promoters to obtain their induction curves (Fig. S2 *Q* and *R*). We modeled these induction curves using the Hill function in Eq. **S10**:

$$\text{Expression} = a \cdot \left(\frac{[\text{inducer}]^n}{k^n + [\text{inducer}]^n} \right) + c. \qquad \textbf{[S10]}$$

In Eq. **S10**, a is the maximum expression in the presence of inducer, n is the Hill coefficient, k is the concentration at which expression is one-half of the maximum, and c is the minimum expression in the absence of inducer. We determined the parameter values by performing a nonlinear least-squares fit of the logarithm of the Hill function to the logarithm of the data (Fig. S2 *Q* and *R*, green curves) and then subtracted *E. coli* autofluorescence (determined by the fluorescence of HL716, which does not have a fluorescent reporter gene) from c to more accurately quantify the amount of "leaky" expression. The resulting values for the parameters for IPTG were as follows: $c = 0.100$ fluorescence a.u., $a = 155$ fluorescence a.u., $k = 176$ μM IPTG, and $n = 3.53$ (unitless). The parameter values for aTc were as follows: $c = 0.419$ fluorescence a.u., $a = 40.7$ fluorescence a.u., $k = 153$ nM aTc, and $n = 5.87$ (unitless).

The above parameter values and Hill functions were used with Eq. **S11** to determine the relative amount of CsrA, CsrB, or CsrD produced at any given amount of IPTG or aTc (i.e., to calibrate the x axis of the transfer functions presented in Figs. 2*D*, 3*D*, and 4*D*):

$$\text{Relative Expression}(\%) = \frac{f([\text{IPTG}])}{a} \cdot 100. \qquad \textbf{[S11]}$$

In Eq. **S11**, f is the Hill function for IPTG induction and a is the maximum expression obtained for the above IPTG induction curve. The relative expression for aTc was calculated in the same manner except that the Hill function and maximum expression associated with aTc were used. The concentration of each of these species is assumed to be proportional to their production rates because the rate constants for the clearance of CsrA, CsrB, and CsrD do not vary under the conditions in which the transfer functions were measured (Figs. 2*D*, 3*D*, and 4*D*, respectively).

1. Levine E, Zhang Z, Kuhlman T, Hwa T (2007) Quantitative characteristics of gene regulation by small RNA. *PLoS Biol* 5(9):e229.
2. Mercante J, Edwards AN, Dubey AK, Babitzke P, Romeo T (2009) Molecular geometry of CsrA (RsmA) binding to RNA and its implications for regulated expression. *J Mol Biol* 392(2):511–528.
3. Gutiérrez P, et al. (2005) Solution structure of the carbon storage regulator protein CsrA from *Escherichia coli*. *J Bacteriol* 187(10):3496–3501.
4. Taniguchi Y, et al. (2010) Quantifying *E. coli* proteome and transcriptome with single-molecule sensitivity in single cells. *Science* 329(5991):533–538.
5. Liu MY, Yang H, Romeo T (1995) The product of the pleiotropic *Escherichia coli* gene csrA modulates glycogen biosynthesis via effects on mRNA stability. *J Bacteriol* 177 (10):2663–2672.
6. Mosteller RD, Goldstein RV, Nishimoto KR (1980) Metabolism of individual proteins in exponentially growing *Escherichia coli*. *J Biol Chem* 255(6):2524–2532.

7. Baker CS, Morozov I, Suzuki K, Romeo T, Babitzke P (2002) CsrA regulates glycogen biosynthesis by preventing translation of glgC in *Escherichia coli*. *Mol Microbiol* 44(6): 1599–1610.
8. Hopkins JF, Panja S, Woodson SA (2011) Rapid binding and release of Hfq from ternary complexes during RNA annealing. *Nucleic Acids Res* 39(12):5193–5202.
9. Gudapaty S, Suzuki K, Wang X, Babitzke P, Romeo T (2001) Regulatory interactions of Csr components: The RNA binding protein CsrA activates csrB transcription in *Escherichia coli*. *J Bacteriol* 183(20):6017–6027.
10. Suzuki K, Babitzke P, Kushner SR, Romeo T (2006) Identification of a novel regulatory protein (CsrD) that targets the global regulatory RNAs CsrB and CsrC for degradation by RNase E. *Genes Dev* 20(18):2605–2617.
11. Weilbacher T, et al. (2003) A novel sRNA component of the carbon storage regulatory system of *Escherichia coli*. *Mol Microbiol* 48(3):657–670.
12. Liu MY, et al. (1997) The RNA molecule CsrB binds to the global regulatory protein CsrA and antagonizes its activity in *Escherichia coli*. *J Biol Chem* 272(28):17502–17510.
13. Kime L, Jourdan SS, Stead JA, Hidalgo-Sastre A, McDowall KJ (2010) Rapid cleavage of RNA by RNase E in the absence of 5′ monophosphate stimulation. *Mol Microbiol* 76 (3):590–604.
14. Redko Y, et al. (2003) Determination of the catalytic parameters of the N-terminal half of *Escherichia coli* ribonuclease E and the identification of critical functional groups in RNA substrates. *J Biol Chem* 278(45):44001–44008.
15. Vellanoweth RL, Rabinowitz JC (1992) The influence of ribosome-binding-site elements on translational efficiency in *Bacillus subtilis* and *Escherichia coli* in vivo. *Mol Microbiol* 6(9):1105–1114.
16. Alon U (2007) *An Introduction to Systems Biology: Design Principles of Biological Circuits* (Chapman and Hall/CRC, Boca Raton, FL).
17. Kim HS, et al. (2013) Distinct binding properties of TIAR RRMs and linker region. *RNA Biol* 10(4):579–589.
18. Fender A, Elf J, Hampel K, Zimmermann B, Wagner EG (2010) RNAs actively cycle on the Sm-like protein Hfq. *Genes Dev* 24(23):2621–2626.
19. Law MJ, Rice AJ, Lin P, Laird-Offringa IA (2006) The role of RNA structure in the interaction of U1A protein with U1 hairpin II RNA. *RNA* 12(7):1168–1178.
20. Goldbeter A, Koshland DE, Jr. (1981) An amplified sensitivity arising from covalent modification in biological systems. *Proc Natl Acad Sci USA* 78(11):6840–6844.
21. Jonas K, et al. (2008) The RNA binding protein CsrA controls cyclic di-GMP metabolism by directly regulating the expression of GGDEF proteins. *Mol Microbiol* 70(1):236–257.
22. Andersen JB, et al. (1998) New unstable variants of green fluorescent protein for studies of transient gene expression in bacteria. *Appl Environ Microbiol* 64(6): 2240–2246.
23. Datsenko KA, Wanner BL (2000) One-step inactivation of chromosomal genes in *Escherichia coli* K-12 using PCR products. *Proc Natl Acad Sci USA* 97(12):6640–6645.
24. Timmermans J, Van Melderen L (2010) Post-transcriptional global regulation by CsrA in bacteria. *Cell Mol Life Sci* 67(17):2897–2908.
25. Wang X, et al. (2005) CsrA post-transcriptionally represses pgaABCD, responsible for synthesis of a biofilm polysaccharide adhesin of *Escherichia coli*. *Mol Microbiol* 56(6): 1648–1663.
26. Lanzer M, Bujard H (1988) Promoters largely determine the efficiency of repressor action. *Proc Natl Acad Sci USA* 85(23):8973–8977.
27. Lutz R, Bujard H (1997) Independent and tight regulation of transcriptional units in *Escherichia coli* via the LacR/O, the TetR/O and AraC/I1-I2 regulatory elements. *Nucleic Acids Res* 25(6):1203–1210.
28. Gardner TS, Cantor CR, Collins JJ (2000) Construction of a genetic toggle switch in *Escherichia coli*. *Nature* 403(6767):339–342.
29. Hussein R, Lim HN (2011) Disruption of small RNA signaling caused by competition for Hfq. *Proc Natl Acad Sci USA* 108(3):1110–1115.
30. Hussein R, Lim HN (2012) Direct comparison of small RNA and transcription factor signaling. *Nucleic Acids Res* 40(15):7269–7279.
31. Shaner NC, et al. (2004) Improved monomeric red, orange and yellow fluorescent proteins derived from *Discosoma* sp. red fluorescent protein. *Nat Biotechnol* 22(12): 1567–1572.

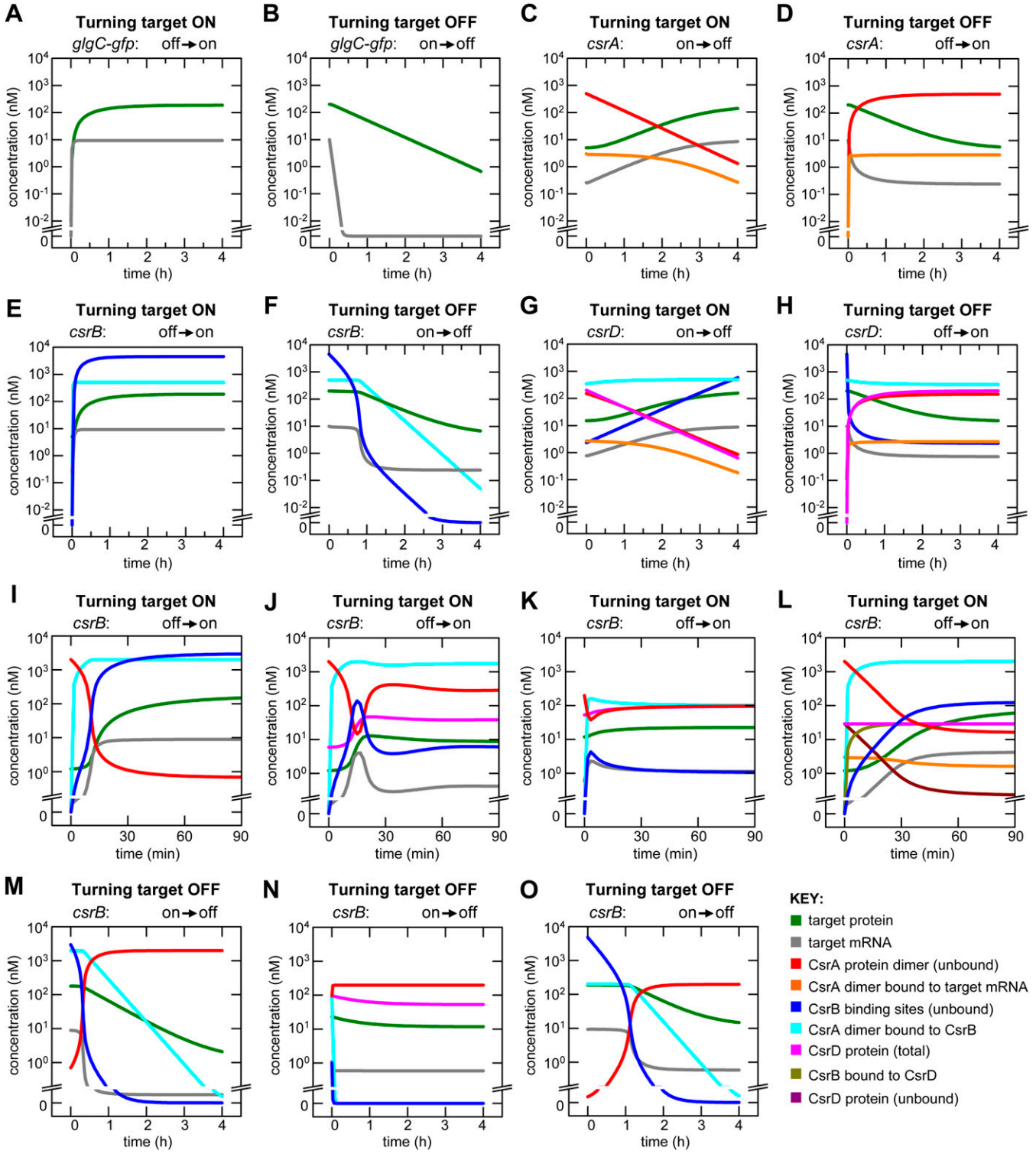

Fig. S1. Simulated concentrations of CsrA cascade components. Components in the CsrA cascade are color coded (key is in the *Bottom Right* of the figure) and not all are shown in each panel. The colors used here do not correspond to those in the main text. (*A* and *B*) Turning on and off *glgC-gfp* mRNA transcription (CsrA, CsrB, and CsrD are absent). These simulations correspond to the gray curves in Figs. 2 *B* and *C*, 3 *B* and *C*, and 4 *B* and *C*. (*C* and *D*) Turning off and on CsrA expression with *glgC-gfp* mRNA at constant maximal transcription (CsrB and CsrD are absent). These simulations correspond to the red curves in Fig. 2 *B* and *C*. (*E* and *F*) Turning on and off CsrB expression with both *glgC-gfp* mRNA and CsrA at constant maximal expression (CsrD is absent). These simulations correspond to the blue curves in Fig. 3 *B* and *C*. (*G* and *H*) Turning off and on CsrD expression with *glgC-gfp* mRNA, CsrA and CsrB all at constant maximal expression. These simulations correspond to the magenta curves in Fig. 4 *B* and *C*. (*I*) Turning on CsrB expression in the synthetic CsrA cascade without feedback and both *glgC-gfp* mRNA and CsrA at constant maximal expression (*csrD* is absent). $[CsrA]_{total} = 1\times$. This simulation corresponds to the control curve (black) in Fig. 6 *E* and *F*. This is a reference panel for comparison with *J*, *K*, and *L*. (*J* and *K*) Turning on CsrB expression in the three-step cascade with negative feedback and saturation of CsrD activity by CsrB (*SI Text*, section 1.5). These simulations correspond to the dark blue and light blue curves in Fig. 6*E*, which have $[CsrA]_{total} = 1\times$ (*J*) and

Legend continued on following page

$[CsrA]_{total} = 0.1\times$ (*K*), respectively. (*L*) Turning on CsrB expression in a system where CsrD is constitutively produced at a low rate (no feedback is present), and *glgC-gfp* mRNA and CsrA are at constant maximal expression. $[CsrA]_{total} = 1\times$. This simulation corresponds to the magenta curve in Fig. 6*F*. (*M*) Turning off CsrB expression in the synthetic CsrA cascade as described in *I*. This simulation corresponds to the control curve (black) in Fig. 6*G*. This is a reference panel for comparison with *N* and *O*. (*N*) Turning off CsrB expression in the cascade as described in *K*. This simulation corresponds to the gold curve in Fig. 6*G*. (*O*) Same as *M* except $[CsrA]_{total} = 0.1\times$.

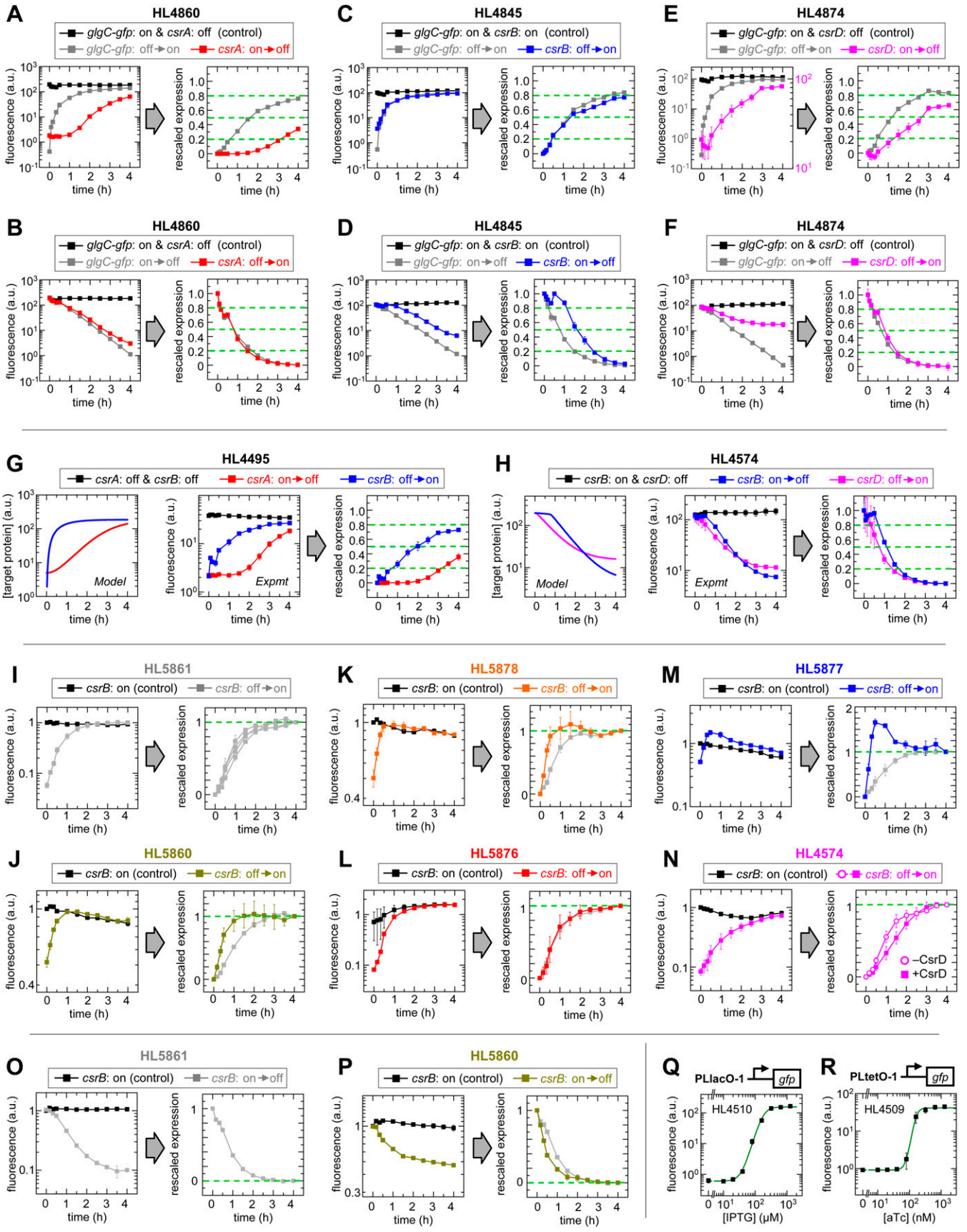

Fig. S2. Normalization and analysis of in vivo dynamics and transfer function data. Error bars are SEM of two or more measurements. (*A*–*F*) Normalization and analysis of data presented in Figs. 2–4. Each left plot is raw data with the physiological control (black curve); each right plot is data from the left plot rescaled to

Legend continued on following page

lie between 0 and 1 (*SI Text*). τ_{20}, τ_{50}, and τ_{80} values (green dashed lines) were calculated as described in the main text using linear interpolation from adjacent data points (Table S2). (*A*) Fig. 2*B* data. (*B*) Fig. 2*C* data. (*C*) Fig. 3*B* data. (*D*) Fig. 3*C* data. (*E*) Fig. 4*B* data. (*F*) Fig. 4*C* data. (*G* and *H*) Longer cascades can signal faster than shorter cascades (under some conditions) within the same strain. Model predictions, raw data, and rescaled data are *Left*, *Center*, and *Right*, respectively. (*G*) CsrA versus CsrB. (*H*) CsrB versus CsrD. (*I*–*P*) Normalization and analysis of data presented in Fig. 6. Each left plot is raw data from two replicates that were rescaled to eliminate constant offsets between them. The black curve is the physiological control. Each right plot is data from the left plot normalized "time point-by-time point" by the physiological control and then rescaled so the initial and final concentrations are 0 and 1 or vice versa (*SI Text*). (*I*) The right plot shows all of the dynamics data for the synthetic cascade that was used as a benchmark for comparison in the right plot of *J*, *K*, *L*, and *M* (gray curve) (note: the synthetic cascade is the same as the black curve shown in Fig. 6 *B*–*E*, respectively). (*J*) Fig. 6*B* data. (*K*) Fig. 6*C* data. (*L*) Fig. 6*D* data. (*M*) Fig. 6*E* data. (*N*) Fig. 6*F* data. (*O*) The right plot shows the dynamics data for the synthetic cascade that was used as a benchmark for comparison in the right plot of *P* (gray curve) (note: the synthetic cascade is the same as the black curve shown in Fig. 6*G*). (*P*) Fig. 6*G* data. (*Q* and *R*) PLlacO-1 (*Q*) and PLtetO-1 (*R*) induction with IPTG and aTc, respectively. Green curves are Hill function fits used to calibrate the *x* axis of the transfer functions in Figs. 2–4.

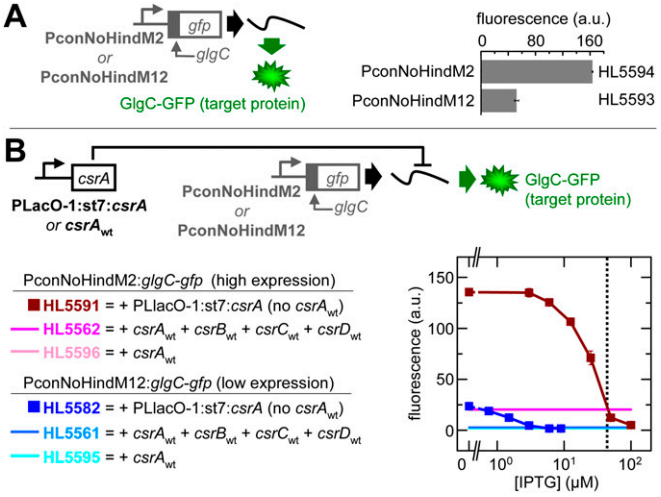

Fig. S3. Effect of target mRNA concentrations on CsrA silencing. Error bars are SEM of duplicate measurements. (*A*) A comparison of the expression of the target mRNA reporter under two different promoters; one has a constitutively high rate of target mRNA transcription (PconNoHindM2), and the other has a lower rate of target mRNA transcription (PconNoHindM12). (*B*) A comparison of the effect of the two different levels of target mRNA expression on the measurement of the CsrA transfer function and native CsrA concentrations. To obtain the transfer functions, we varied the level of induction of the PLlacO-1:st7:*csrA* gene and measured its effect on target protein expression with the PconNoHindM2:*glgC-gfp* reporter or the PconNoHindM12:*glgC-gfp* reporter. To assess the effect of the native *csrA* ("$csrA_{wt}$"), we measured the expression of both reporters in strains with the complete native *csrA* system (+ $csrA_{wt}$ + $csrB_{wt}$ + $csrC_{wt}$ + $csrD_{wt}$) or with only native *csrA* (+ $csrA_{wt}$). The synthetic system with PLlacO-1:st7:*csrA* and high levels of target mRNA transcription (PconNoHindM2:*glgC-gfp*) achieved an amount of target protein expression that was similar to the native *csrA* at 25–50 μM IPTG (black dotted line), which is ∼10% of the maximum CsrA that we induced (Fig. 2*D*). In contrast, with the synthetic system with PLlacO-1:st7:*csrA* and lower levels of target mRNA transcription (PconNoHindM12:*glgC-gfp*), we could not accurately determine native CsrA levels because the lower quantity of target mRNA meant that it was completely silenced by CsrA at concentrations less than the native concentration (i.e., it was fully silenced at <10 μM IPTG).

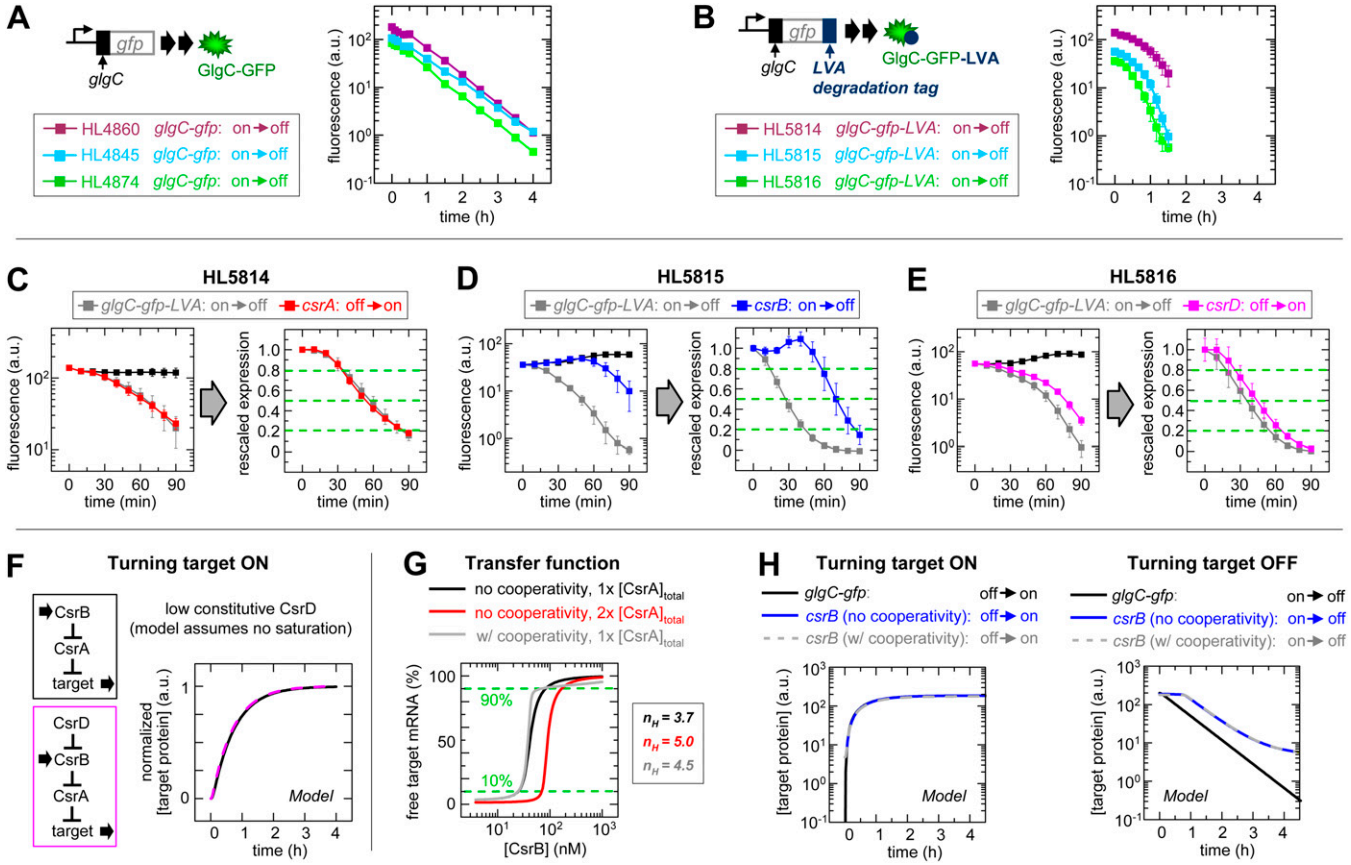

Fig. S4. Alternate experimental and model designs. (*A–E*) Dynamics experiments using target protein without (passive clearance of the target protein) and with the LVA degradation tag (active and passive clearance of the target protein). Transcription of the target gene is turned off at $t = 0$. (*A*) Clearance of GlgC-GFP without the degradation tag. Dynamics data from Figs. 2*C*, 3*C*, and 4*C* are replotted for comparison. (*B*) Clearance of GlgC-GFP with the LVA degradation tag. Data are replotted in *B–D*. Note: the curves no longer have a predictable linear decay on a logarithmic plot, and instead degradation is initially slow and then becomes faster as the concentration of target protein decreases. (*C–E*) Experiments with a target protein without the LVA tag in Figs. 2*C*, 3*C*, and 4*C* repeated with a target protein that has the LVA tag in *C*, *D*, and *E*, respectively. The green dashed lines indicate 80%, 50%, and 20% of maximum expression. (*F*) Simulated induction of *csrB* in the presence or absence of a low CsrD concentration without negative feedback (pink dashed and black curves, respectively). Simulations were performed using the "three-step cascade" model that does not include the CsrB–CsrD complex (*SI Text*, section 1.4). (*G* and *H*) Simulations demonstrating that cooperativity has negligible effect on the steady state and dynamic behavior of the CsrA system. (*G*) Free target mRNA levels as a function of CsrB concentration (i.e., CsrB transfer functions). CsrB has nine sites for CsrA dimers. There are three comparisons: (*i*) CsrA dimers bind independently at 1× concentration (black); (*ii*) CsrA dimers bind independently but are present at twice the concentration (2×) (red); and (*iii*) CsrA dimers bind cooperatively at 1× concentration (gray) to CsrB (*SI Text*). n_H is the Hill coefficient that would produce a Hill function with the same "steepness" as the function shown; steepness was measured using the levels of CsrB required to reach 10% and 90% occupancy of the target mRNA by CsrA (green dashed lines) (*SI Text*). (*H*) Dynamics of target protein expression following the turning on and off *glgC-gfp* transcription or the transcription of CsrB (thereby turning target expression on and off, respectively), with and without cooperative binding between CsrA dimers and CsrB. Direct induction of target protein expression is provided for comparison.

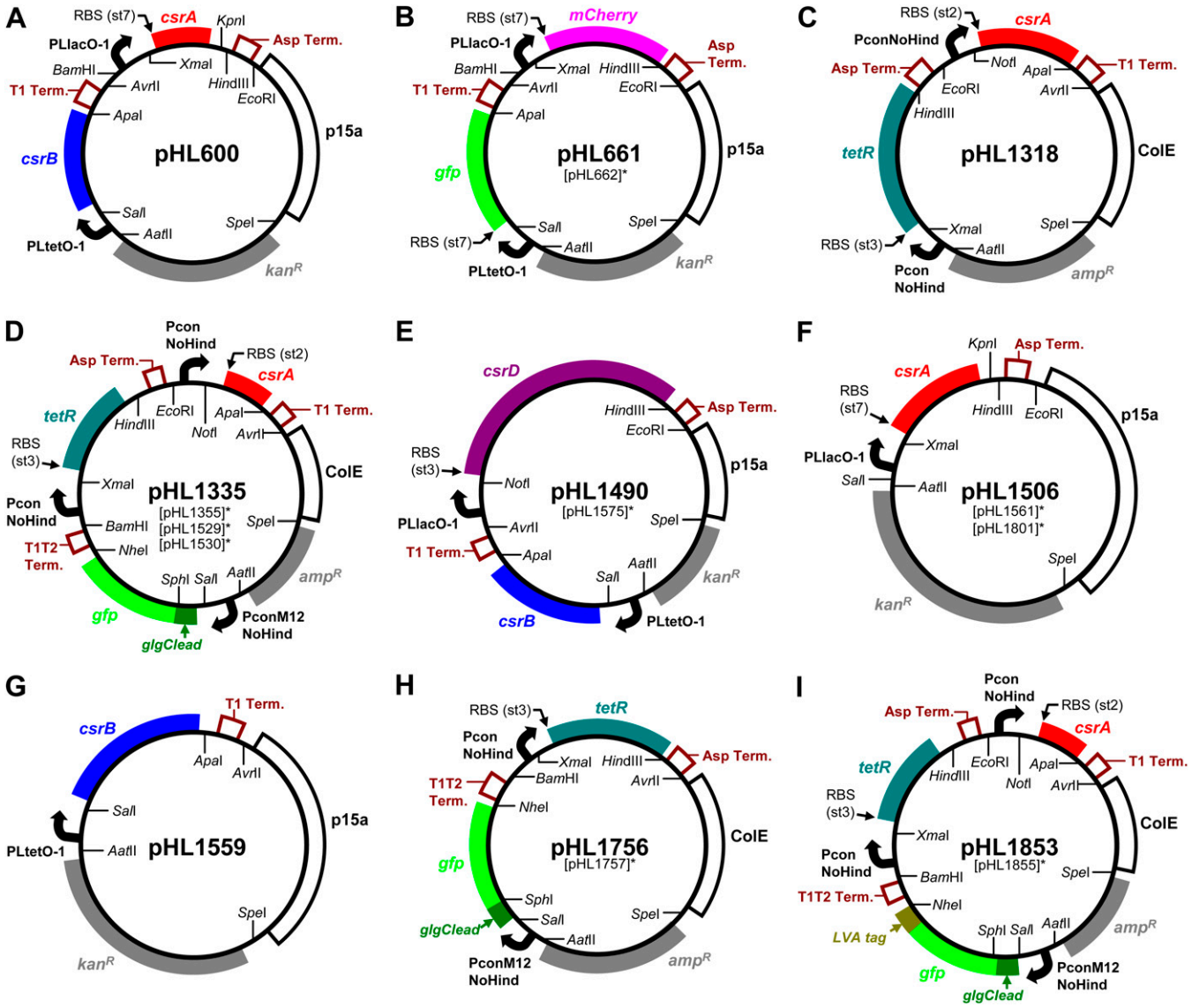

Fig. S5. Plasmid maps. *Plasmids listed in brackets are similar to the plasmid shown except for the differences described here. Relative expression levels from the different ribosome binding sequence (RBS) used: st7 > st3 > st2. p15a and ColE are origins of replication. T1 Term, T1T2 Term and Asp Term are terminator sequences. (*A*) pHL600. (*B*) pHL661. In pHL662, the st7-*gfp* replaces st7-*mCherry* and st7-*mCherry* replaces st7-*gfp*. (*C*) pHL1318. (*D*) pHL1335. In pHL1355, the st3 RBS replaces st2 for *csrA*. In pHL1529, PLlacO-1 replaces PconNoHindM12. In pHL1530, st3 replaces st2 and PLlacO-1 replaces PconNoHindM12. (*E*) pHL1490. In pHL1575, PconNoHind replaces PLtetO-1 and PLtetO-1 replaces PLacO-1. (*F*) pHL1506. In pHL1561, PLtetO-1 replaces PLlacO-1 (SalI is removed). In pHL1801, *gfp* replaces *csrA*. (*G*) pHL1559. (*H*) pHL1756. In pHL1757, a stronger PconM2NoHind promoter replaces PconM12NoHind. (*I*) pHL1853. In pHL1855, st3 replaces st2 for *csrA*.

Table S1. Initial conditions for dynamic simulations

Simulation	[GFP], nM	[m], nM	[A], nM	[Am], nM	[B], nM	[AB], nM	[D], nM	[BD], nM
Fig. 2*B*, *glgC-gfp* turned on	0	0	0	0	n/a	n/a	n/a	n/a
Fig. 2*B*, *csrA* turned off	5	0.26	497	3	n/a	n/a	n/a	n/a
Fig. 2*C*, *glgC-gfp* turned off	200	10	0	0	n/a	n/a	n/a	n/a
Fig. 2*C*, *csrA* turned on	200	10	0	0	n/a	n/a	n/a	n/a
Fig. 3*B*, *glgC-gfp* turned on	0	0	0.11	0	4,500	500	n/a	n/a
Fig. 3*B*, *csrB* turned on	5	0.26	497	3	0	0	n/a	n/a
Fig. 3*C*, *glgC-gfp* turned off	198	9.9	0.11	0.026	4,500	500	n/a	n/a
Fig. 3*C*, *csrB* turned off	198	9.9	0.11	0.026	4,500	500	n/a	n/a
Fig. 4*B*, *glgC-gfp* turned on	0	0	0.11	0	4,500	500	0	n/a
Fig. 4*B*, *csrD* turned off	15	0.76	150	2.7	2.3	347	200	n/a
Fig. 4*C*, *glgC-gfp* turned off	198	9.9	0.11	0.026	4,500	500	0	n/a
Fig. 4*C*, *csrD* turned on	198	9.9	0.11	0.026	4,500	500	0	n/a
Fig. 6 *E* and *F*, control (black)	1.2	0.06	1,997	3	0	0	0	0
Fig. 6*E*, 1.0× CsrA (dark blue)	1.2	0.06	1,997	3	0	0	5.9	0
Fig. 6*E*, 0.1× CsrA (light blue)	11.8	0.6	197	3	0	0	53	0
Fig. 6*F*, fixed CsrD (magenta)	1.2	0.06	1,997	3	0	0	29	0
Fig. 6*G*, control (black)	178	8.9	0.7	0.1	3,000	1,999	0	0
Fig. 6*G*, native system (gold)	22.8	1.1	95	2.6	1	102	47	49
Fig. S2*O*, native without *csrD*	187	9.3	0.042	0.009	4,800	200	0	0

The initial conditions for each simulation performed in the main text are included here. [GFP], [m], [A], [Am], [B], [AB], [D], and [BD] represent the concentrations of the target protein, the target mRNA, CsrA dimers, the CsrA–target mRNA complex, CsrB, the CsrA–CsrB complex, CsrD, and the CsrB–CsrD complex, respectively, as described (*SI Text*); n/a (not applicable) indicates that the species was not included in the model.

Table S2. Synthetic circuit signaling times

Figure	Experiment	τ_{20}, min	τ_{50}, min	τ_{80}, min
Fig. 2*B* (turning target on)	*glgC-gfp* turned on	39 ± 1	97 ± 1	>240
	csrA turned off	187 ± 1	>240	>240
Fig. 3*B* (turning target on)	*glgC-gfp* turned on	27 ± 1	74 ± 1	196 ± 3
	csrB turned on	26 ± 1	81 ± 2	>240
Fig. 4*B* (turning target on)	*glgC-gfp* turned on	28 ± 1	72 ± 2	159 ± 6
	csrD turned off	77 ± 18	158 ± 5	>240
Fig. S2*G* (turning target on)	*csrA* turned off	190 ± 9	>240	>240
	csrB turned on	44 ± 9	119 ± 18	>240
Fig. 2*C* (turning target off)	*glgC-gfp* turned off	90 ± 1	47 ± 1	9 ± 1
	csrA turned on	103 ± 3	49 ± 1	8 ± 3
Fig. 3*C* (turning target off)	*glgC-gfp* turned off	89 ± 2	46 ± 2	13 ± 1
	csrB turned off	147 ± 4	97 ± 9	67 ± 3
Fig. 4*C* (turning target off)	*glgC-gfp* turned off	78 ± 1	41 ± 1	14 ± 1
	csrD turned on	88 ± 7	52 ± 4	17 ± 2
Fig. S2*H* (turning target off)	*csrB* turned off	103 ± 1	67 ± 2	42 ± 4
	csrD turned on	83 ± 3	42 ± 12	16 ± 19
Fig. S4*C* (turning target off)	*glgC-gfp* turned off	85 ± 7	57 ± 6	35 ± 5
	csrA turned on	86 ± 1	54 ± 2	33 ± 2
Fig. S4*D* (turning target off)	*glgC-gfp* turned off	44 ± 3	27 ± 2	14 ± 3
	csrB turned off	~ 90	70 ± 7	58 ± 6
Fig. S4*E* (turning target off)	*glgC-gfp* turned off	55 ± 5	35 ± 6	18 ± 8
	csrD turned on	65 ± 4	43 ± 6	25 ± 8

The τ_{20}, τ_{50}, and τ_{80} values for turning on and off target gene expression (calculated from normalized dynamics data shown in Figs. S2 and S4). Uncertainty represents the SEM of duplicate measurements.

Table S3. Plasmids and strains

ID*	Description
pHL177	Contains chloramphenicol resistance cassette flanked by FRT sites
pHL600	PLtetO-1:*csrB*, PLlacO-1:RBS(st7):*csrA*
pHL661	PLtetO-1:RBS(st7):*gfp*, PLlacO-1:RBS(st7):*mCherry*
pHL662	PLtetO-1:RBS(st7):*mCherry*, PLlacO-1:RBS(st7):*gfp*
pHL1318	PconNoHind:RBS(st3):*tetR*, PconNoHind:RBS(st2):*csrA*
pHL1335	PconNoHindM12:*glgC*::*gfp*†, PconNoHind:RBS(st3):*tetR*, PconNoHind:RBS(st2):*csrA*
pHL1355	PconNoHindM12:*glgC*::*gfp*†, PconNoHind:RBS(st3):*tetR*, PconNoHind:RBS(st3):*csrA*
pHL1490	PLtetO-1:*csrB*, PLlacO-1:RBS(st3):*csrD*
pHL1506	PLlacO-1:RBS(st7):*csrA*
pHL1529	PLlacO-1:*glgC*::*gfp*†, PconNoHind:RBS(st3):*tetR*, PconNoHind:RBS(st2):*csrA*
pHL1530	PLlacO-1:*glgC*::*gfp*†, PconNoHind:RBS(st3):*tetR*, PconNoHind:RBS(st3):*csrA*
pHL1559	PLtetO-1:*csrB*
pHL1561	PLtetO-1:RBS(st7):*csrA*
pHL1575	PconNoHind:*csrB*, PLtetO-1:RBS(st3):*csrD*
pHL1756	PconNoHindM12:*glgC*::*gfp*†, PconNoHind:RBS(st3):*tetR*
pHL1757	PconNoHindM2:*glgC*::*gfp*†, PconNoHind:RBS(st3):*tetR*
pHL1801	PLlacO-1:RBS(st7):*gfp*
pHL1853	PLlacO-1:*glgC*::*gfp*::*LVA*†, PconNoHind:RBS(st3):*tetR*, PconNoHind:RBS(st2):*csrA*
pHL1855	PLlacO-1:*glgC*::*gfp*::*LVA*†, PconNoHind:RBS(st3):*tetR*, PconNoHind:RBS(st3):*csrA*
HL3721	HL716‡ + Δ*csrB* + Δ*csrC* + Δ*glgCAP* + Δ*pgaABCD*
HL3796	HL716‡ + Δ*csrA* + Δ*csrB* + Δ*csrC* + Δ*glgCAP* + Δ*pgaABCD*
HL4018	HL716‡ + Δ*csrB* + Δ*csrC* + Δ*csrD* + Δ*glgCAP* + Δ*pgaABCD*
HL4142	HL716‡ + Δ*csrA* + Δ*csrB* + Δ*csrC* + Δ*csrD* + Δ*glgCAP* + Δ*pgaABCD*
HL4495	HL4142 + pHL1335 + pHL600
HL4509	HL4142 + pHL1318 + pHL661
HL4510	HL4142 + pHL1318 + pHL662
HL4574	HL4142 + pHL1355 + pHL1490
HL4845	HL4142 + pHL1530 + pHL1559
HL4860	HL4142 + pHL1529 + pHL1561
HL4874	HL4142 + pHL1530 + pHL1575
HL5561	MG1655 + pHL1756
HL5562	MG1655 + pHL1757
HL5582	HL4142 + pHL1506 + pHL1756
HL5591	HL4142 + pHL1506 + pHL1757
HL5593	HL4142 + pHL1756
HL5594	HL4142 + pHL1757
HL5595	HL4018 + pHL1756
HL5596	HL4018 + pHL1757
HL5814	HL4142 + pHL1561 + pHL1853
HL5815	HL4142 + pHL1559 + pHL1855
HL5816	HL4142 + pHL1575 + pHL1855
HL5840	HL716‡ + Δ*pgaABCD*
HL5860	HL5840 + pHL1559 + pHL1756
HL5861	HL4142 + pHL1559 + pHL1355
HL5876	HL4018 + pHL1559 + pHL1756
HL5877	HL3796 + pHL1559 + pHL1355
HL5878	HL3721 + pHL1559 + pHL1756
HL5944	HL3796 + pHL1801
HL5947	HL4142 + pHL1561

Selected plasmids and strains were submitted to the Addgene repository (www.addgene.org).

*ID numbers beginning with "pHL" correspond to plasmids; ID numbers beginning with "HL" correspond to strains.

†To construct the *glgC*::*gfp* reporter gene, the DNA sequence of the *glgCAP* mRNA between −61 and +8 nucleotides (relative to the *glgC* start codon) was translationally fused to the *gfp* coding region.

‡This strain is MG1655 with $lacI_q$ added to the chromosome (1).

1. Hussein R, Lim HN (2011) Disruption of small RNA signaling caused by competition for Hfq. *Proc Natl Acad Sci USA* 108(3):1110–1115.

Table S4. Oligonucleotides

Name	Description	Sequence
csrAKOpkD1F	For deletion of *csrA* using pHL177 as template	TGCCGGGATACAGAGAGACCCGACTCTTTTAATCTTTC AAGGAGCAAAGAGTGTAGGCTGGAGCTGCTTC
csrAKOpkD4R	For deletion of *csrA* using pHL177 as template	GGAGAAATTTTGAGGGTGCGTCTCACCGATAAAGATGAGAC GCGGAAAGAATTCCGGGGATCCGTCGACC
csrBKOpkD1F	For deletion of *csrB* using pKD13 as template	AGCGCCTTGTAAGACTTCGCGAAAAAGACGATTCTAT CTTCGTCGACAGGGTGTAGGCTGGAGCTGCTTC
csrBKOpkD4R	For deletion of *csrB* using pKD13 as template	GTGGTCATAAAGCAACCTCAATAAGAAAAACTGCCGCGA AGGATAGCAGGATTCCGGGGATCCGTCGACC
csrCKOpkD1F	For deletion of *csrC* using pKD13 as template	ACTGATGGCGGTTGATTGTTTGTTTAAAGCAAAGGCGT AAAGTAGCACCCGTGTAGGCTGGAGCTGCTTC
csrCKOpkD4R	For deletion of *csrC* using pKD13 as template	GCCGTTTTATTCAGTATAGATTTGCGGCGGAATCTAACA GAAAGCAAGCAATTCCGGGGATCCGTCGACC
csrDpkD1F	For deletion of *csrD* using pKD13 as template	ATCTGATTTGCTAGTATGCCCGCTTCCTCACTATCGGAGTT AACACAAGGGTGTAGGCTGGAGCTGCTTC
csrDpkD4R	For deletion of *csrD* using pKD13 as template	CATGAGACGCAGCGCGCATTATTCTACGTGAAAACGGATT AAACGGCAGGATTCCGGGGATCCGTCGACC
glgCpkD1F	For deletion of *glgCAP* using pKD13 as template	CCTGCACACGGATTGTGTGTGTTCCAGAGATGATAAAAAA GGAGTTAGTCGTGTAGGCTGGAGCTGCTTC
glgPpkD4R	For deletion of *glgCAP* using pKD13 as template	TTACAATCTCACCGGATCGATATGCCAGATATGATCGGC GTACTCTTTGAATTCCGGGGATCCGTCGACC
pgaApkD4R	For deletion of *pgaABCD* using pKD13 as template	CTGTAATTAGATACAGAGAGAGATTTTGGCAATACATG GAGTAATACAGGATTCCGGGGATCCGTCGACC
pgaDpkD1F	For deletion of *pgaABCD* using pKD13 as template	AGTGTGTTATCGGTGCAGAGCCCGGGCGAACCGGGCTT TGTTTTGGGTGTGTGTAGGCTGGAGCTGCTTC
csrARBSXmaF	PCR amplifies *csrA* with a synthetic RBS (st7)	CCTCCCGGGTAAGGAGGAAAAAAAATGCTGATTCTG ACTCGTCGAGTTG
csrAKpnHindR	PCR amplifies *csrA*	GGCCAAGCTTCTTTCAGGTACCTTAGTAACTGGACTG CTGGGATTTTTCAG
csrBSalF	PCR amplifies *csrB*	CAAGTCGACGAGTCAGACAACGAAGTGAACATC
csrBApaR	PCR amplifies *csrB*	CATGGGCCCAATAAAAAAAGGGAGCACTGTATTCACAGC
csrARBS2NotIF	PCR amplifies *csrA* with a synthetic RBS (st2)	TCCTGCGGCCGCTAAGGAGGAAATGCTGATTCTGACTC GTCGAGTTG
csrARBS3NotIF	PCR amplifies *csrA* with a synthetic RBS (st3)	TCCTGCGGCCGCTAAGGAGGAAAATGCTGATTCTGAC TCGTCGAGTTG
csrAApaR	PCR amplifies *csrA*	TAAGGGCCCTTAGTAACTGGACTGCTGGGATTTTTCAG
glgCleadSalF	PCR amplifies 5′UTR of *glgC* leader for fusion to *gfp*	CCTGTCGACTCTGGCAGGGACCTGCACACGGATTG
glgCleadSphR	PCR amplifies 5′UTR of *glgC* for fusion to *gfp*	TACGCATGCTAACCATGACTAACTCCTTTTTTATCATCTCTGG
GFPRBSSalSphF	PCR amplified *gfp* with SalI & SphI sites	TTAGTCGACTAAGGAGGAAAAAGCATGCGTAAAGG AGAAGAACTTTTC
PconNoHindBamHF	PCR synthesis of Pcon promoter with no HindIII site	CGCGGATCCTCGAGCACCGTCGTTGTTGACATTTTTAT GCTTGGCGGTTATAAT
PconNoHindXmaR	PCR synthesis of Pcon promoter with no HindIII site	CCTCCCGGGTGTGTGGAATCCATTATAACCGCCAAGCA TAAAAATGTCAACAAC
PconNoHindEcoRF	PCR synthesis of Pcon promoter with no HindIII site	CCGGAATTCTCGAGCACCGTCGTTGTTGACATTTTTAT GCTTGGCGGTTATAAT
PconNoHindNotIR	PCR synthesis of Pcon promoter with no HindIII site	TCCTGCGGCCGCCTGTGTGGAATCCATTATAACCGCC AAGCATAAAAATGTCAACAAC
PconM2NoHindAatF	PCR synthesis of PconM2 promoter with no HindIII site	CGCGACGTCTCGAGCACCGTCGTTGTTTACATTTTTAT GCTTGGCGGTTATGAT
PconM2NoHindSalR	PCR synthesis of PconM2 promoter with no HindIII site	TTAGTCGACCTGTGTGGAATCCATCATAACCGCCAAGC ATAAAAATGTAAACAAC
PconM8NoHindAatF	PCR synthesis of PconM12 promoter with no HindIII site	CGCGACGTCTCGAGCACCGTCGTTGTTTACATTTTTAT GCTTGGCGGTTATGGT
PconM12NoHindSalR	PCR synthesis of PconM12 promoter with no HindIII site	TTAGTCGACCTGTGTGGAATCCACCATAACCGCCAAGC ATAAAAATGTAAACAAC
PconNoHindBamHF	PCR synthesis of Pcon promoter with no HindIII site	CGCGGATCCTCGAGCACCGTCGTTGTTGACATTTTTAT GCTTGGCGGTTATAAT
csrDRBS3NotIF	PCR amplifies *csrD* with a synthetic RBS (st3)	TCCTGCGGCCGCTAAGGAGGAAAATGAGATTAACGA CGAAATTTTCG
csrDHindR	PCR amplifies *csrD*	GCCAAGCTTTTAAACCGAGTATCTTTGTGAATA
csrDinF	For RT-PCR measurement of *csrD* mRNA	CTGGCGCGTTACCACCGCAGTGAT
csrDinR	For RT-PCR measurement of *csrD* mRNA	CCAATGTGGATCATATCGTCGCGA

Oligonucleotides were used (*i*) to construct the plasmids, (*ii*) to create PCR products for the deletion of CsrA system components from the chromosome, or (*iii*) to perform quantitative RT-PCR measurements of intracellular mRNA concentrations.